






# Observation of accurately designed bound states in the continuum in momentum space

JIAJU WU,<sup>1,†</sup> JINGGUANG CHEN,<sup>2,†</sup> XIN QI,<sup>1</sup> ZHIWEI GUO,<sup>1</sup>  JIAJUN WANG,<sup>2</sup> FENG WU,<sup>3</sup>  YONG SUN,<sup>1</sup>   
YUNHUI LI,<sup>1</sup> HAITAO JIANG,<sup>1,4</sup>  LEI SHI,<sup>2,5</sup>  JIAN ZI,<sup>2</sup> AND HONG CHEN<sup>1</sup>

<sup>1</sup>MOE Key Laboratory of Advanced Micro-Structured Materials, School of Physics Science and Engineering, Tongji University, Shanghai 200092, China

<sup>2</sup>State Key Laboratory of Surface Physics, Key Laboratory of Micro- and Nano-Photonic Structures (Ministry of Education) and Department of Physics, Fudan University, Shanghai 200433, China

<sup>3</sup>School of Optoelectronic Engineering, Guangdong Polytechnic Normal University, Guangzhou 510665, China

<sup>4</sup>e-mail: jiang-haitao@tongji.edu.cn

<sup>5</sup>e-mail: lshi@fudan.edu.cn

<sup>†</sup>These authors contributed equally to this work.

Received 15 December 2023; revised 22 January 2024; accepted 24 January 2024; posted 26 January 2024 (Doc. ID 515969); published 13 March 2024

**Bound states in the continuum (BICs) in artificial photonic structures have received considerable attention since they offer unique methods for the extreme field localization and enhancement of light-matter interactions. Usually, the symmetry-protected BICs are located at high symmetric points, while the positions of accidental BICs achieved by tuning the parameters will appear at some points in momentum space. Up to now, to accurately design the position of the accidental BIC in momentum space is still a challenge. Here, we theoretically and experimentally demonstrate an accurately designed accidental BIC in a two-coupled-oscillator system consisting of bilayer gratings, where the optical response of each grating can be described by a single resonator model. By changing the interlayer distance between the gratings to tune the propagation phase shift related to wave vectors, the position of the accidental BIC can be arbitrarily controlled in momentum space. Moreover, we present a general method and rigorous numerical analyses for extracting the polarization vector fields to observe the topological properties of BICs from the polarization-resolved transmission spectra. Finally, an application of the highly efficient second harmonic generation assisted by quasi-BIC is demonstrated. Our work provides a straightforward strategy for manipulating BICs and studying their topological properties in momentum space.** © 2024 Chinese Laser Press

<https://doi.org/10.1364/PRJ.515969>

## 1. INTRODUCTION

Bound states in the continuum (BICs) are an exception to conventional bound states. They lie inside the continuum and coexist with extended states, but they remain perfectly localized without any radiation [1]. Although BICs were first proposed by von Neumann and Wingner in quantum mechanisms [2], they are general solutions of wave equations and have since been identified in various systems [3–7]. By introducing external perturbations or adjusting parameters of the system, a true BIC will collapse to sharp Fano resonance with ultrahigh quality ( $Q$ ) factor that is called quasi-BIC [8–11], which can boost light-matter interactions for practical applications in a variety of lasing [12–14], biosensors [15–17], unidirectional transfer [18,19], nonlinear devices [20–22], and enhancement of optical chirality [23–28].

As singular points of polarization in momentum space, the topological properties of BICs ensure that they can be

continuously shifted in momentum space [29]. By merging multiple BICs at different places of momentum space, the problem of scattering losses induced by fabrication imperfections can be effectively overcome [22,29,30]. Besides, by breaking the symmetry of the system or adjusting the structural parameters, various evolution phenomena including the generation and annihilation of BICs have been observed [29–33]. Different BICs can be categorized with respect to the physical origin of far-field radiation suppression. When a system possesses a reflection or rotational symmetry, the modes with different symmetry classes are completely decoupled. A bound state of one symmetry class can be embedded in the continuous spectrum of another symmetry class, where their coupling is forbidden as long as the symmetry is preserved. This kind of BIC is called symmetry-protected BIC [1,10], which appears in a variety of photonic structures such as metasurfaces [10,11,25,34–37], photonic crystal slabs [38–41], gratings

[18,42–44], photonic wave-guides [45,46], and so on. Compared with the symmetry-protected BIC, the accidental BIC obtained by tuning the parameters of the system stems from the complete suppression of the radiation of the bound state into the continuous channels [8,46]. In many cases, some accidental BICs are known as Friedrich-Wintgen (FW) BIC [8], which can be interpreted as destructive interference in two radiating channels from two coupled resonators of a system [47–50]. When the two resonators in the system are separated in some distance, the accidental BIC becomes a Fabry–Perot (FP) BIC [1,6,47]. Interestingly, the formation condition of FP BICs is just the standing wave condition when the accumulated propagation phase shift of the wave after the round-trip is the integer multiple of  $2\pi$ . In general, the symmetry-protected BICs are fixed at highly symmetric points in momentum space [10,11,34], while the position of accidental BICs strongly depends on the geometric parameters [1,22,30,32]. Up to now, to accurately design the position of the accidental BIC in momentum space by demand remains an open question.

In this paper, we propose bilayer gratings as a coupled-oscillators system to realize an accurately designed F-P BIC in momentum space. We show that the position of the F-P BIC can be freely designed in momentum space by changing the interlayer distance between the gratings to tune the propagation phase shift related to wave vectors. We further study the evolution of BICs in momentum space. Particularly, we propose a general approach for extracting the polarization vector fields to observe the topological properties of BICs from the transmission spectra. Finally, as an example of application, the highly efficient second harmonic generation assisted by quasi-BIC is demonstrated. Our work offers a route to accurately design accidental BICs, which is very useful in the applications of BICs.

## 2. PRINCIPLE AND DESIGN

The FP BIC is a type of accidental BIC obtained through parameter tuning, which is commonly found in systems with two resonances coupled to the same radiation channel. Figure 1 shows the typical theoretical model. We consider two resonance amplitudes  $A = (A_1, A_2)^T$  evolving in time as  $i\partial A/\partial t = HA$ . According to temporal coupled-mode theory, the Hamiltonian can be written as follows [1]:

$$H = \begin{pmatrix} \omega_1 & \kappa \\ \kappa & \omega_2 \end{pmatrix} - i \begin{pmatrix} \gamma_1 & \sqrt{\gamma_1\gamma_2}e^{i\varphi} \\ \sqrt{\gamma_1\gamma_2}e^{i\varphi} & \gamma_2 \end{pmatrix}, \quad (1)$$

where  $\kappa$  and  $\sqrt{\gamma_1\gamma_2}e^{i\varphi}$  are the near-field coupling and far-field coupling, respectively. Here  $\varphi$  is the propagation phase

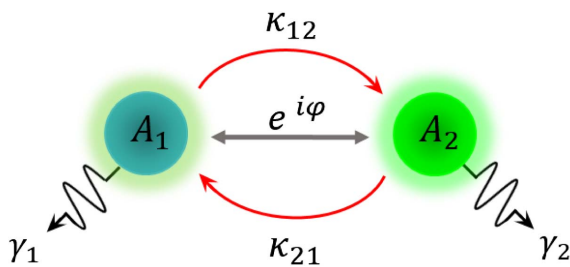


Fig. 1. Theoretical model of the two-coupled-oscillator system.

shift between two resonances. Herein, the resonance frequencies of two resonators are identical. The two eigenvalues of  $H$  are

$$\omega_{\pm} = \omega_0 \pm \kappa - i\gamma(1 \pm e^{i\varphi}), \quad (2)$$

and the real and the imaginary parts of two eigenmodes are

$$\text{Re}(\omega_{\pm}) = \omega_0 \pm (\kappa + \gamma \sin \varphi), \quad (3)$$

$$\text{Im}(\omega_{\pm}) = \gamma(1 \pm \cos \varphi).$$

We can further obtain the formation condition of the BIC,

$$\varphi = k_0 n d \cos \theta = m\pi \quad (m \text{ is an integer}), \quad (4)$$

where  $k_0$  represents the wave vector of the single resonator in the direction of propagation,  $\theta$  is the incident angle, and  $n$  and  $d$  denote the refractive index of the background and distance between two resonances, respectively. When  $\varphi = k_0 n d \cos \theta = m\pi$ , i.e., satisfying the BIC condition, one of the two eigenmodes becomes a BIC with a purely real eigenfrequency, and the other eigenmode becomes more lossy with twice the original decay rate. Notice that the propagation phase shift related to vectors can be flexibly tuned by changing the interlayer distance between two resonators. As a result, the formation condition of the BIC can be maintained for different wave vectors. In other words, the position of the BIC can be arbitrarily designed in momentum space.

For a real structure, the optical features of resonant guided modes in grating can be described by using coupled-mode theory. Around the resonance frequency, the electromagnetic response of the grating can be considered as a single resonator model (SRM) [51]. Herein, we consider a two-coupled-resonator model consisting of two identical one-dimensional dielectric gratings as a common platform to demonstrate that such a BIC can be freely designed in momentum space. Figure 2(a) shows the schematic of the proposed structure in which the width and height of infinitely long bars with gaps are  $w = 0.5a$  and  $b = 0.54a$ , respectively, where  $a$  is the lattice constant. The interlayer distance between the gratings is denoted by  $d$ , and the dielectric constant is  $\epsilon_r = 2$ . In general, the resonant responses of the grating exhibit an asymmetrical Fano line shape. To better consider the grating as a resonator, we select the proper material with low refractive indices contrast compared to the background. Herein, we first calculate the dispersion relation of the single grating for the transverse magnetic (TM) polarization, as shown in Fig. 2(b). It can be seen that the resonance frequency will decrease as the incident angle increases. Besides, the optical response of single grating can be described by the SRM around the angular frequency of the guided mode resonances (GMRs). According to the SRM, the reflectance can be expressed as  $R(\omega, \omega_0, \gamma_0) = \gamma_0^2 / (\omega_0^2 - \omega^2) - \gamma_0^2$  [51], where  $\omega_0 a / 2\pi c = 0.727$  and  $\gamma_0 a / 2\pi c = 0.0276$ . By fitting the reflectance spectrum of single grating by the SRM at  $k_x a / 2\pi = 0.122$ , one can see that the optical features of single grating around the resonance frequency match well with the SRM (see Appendix A). Thus, the optical response of single grating can be described by a single resonator model. Next, a freely designed BIC will be revealed in two-coupled-oscillator system consisting of bilayer gratings.

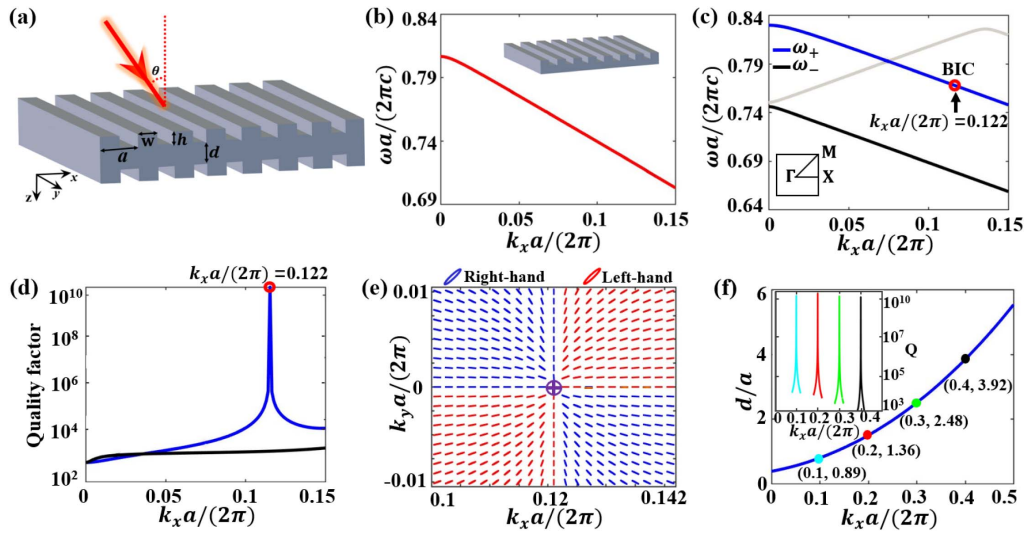


**Fig. 2.** (a) Schematic of the bilayer grating for a freely designed BIC. (b) Dispersion relation of single layer grating. (c) Band structure of the bilayer grating at  $d/a = 0.99$ . The red circle represents the position of  $k_x a/2\pi = 0.122$ . (d) The corresponding  $Q$  factors. (e) Far-field polarization states around BIC. (f) The dependence of BICs on the interlayer distance  $d$  and  $k_x a/2\pi$ . The inset gives  $Q$  factors around the four BIC modes ( $\omega_+$ ) for four different interlayer distances indicated by the color points.

Now, we demonstrate that the BIC supported by bilayer gratings can be designed by adjusting the interlayer distance between two gratings. Based on the formation condition of BIC, one can expect the emergence of BIC by designing suitable interlayer distance at arbitrary wave vectors. For instance, when  $\theta = 10^\circ$  (i.e.,  $k_x a/2\pi = 0.122$ ) and  $m = 1$ , the interlayer distance  $d = 0.99a$  can be obtained from Eq. (4). The calculated band structures of bilayer gratings at  $d/a = 0.99$  is shown in Fig. 2(c), where the bands above and below correspond to  $\omega_+$  and  $\omega_-$  bands, respectively. In this case,  $\omega_+$  becomes a BIC with a purely real eigenfrequency at  $k_x a/2\pi = 0.122$ . Notice that there is another band marked by the gray solid line, which stems from Brillouin zone folding. Figure 2(d) shows the  $Q$  factors distribution of two modes along the  $\Gamma X$  direction, in which a BIC with infinite  $Q$  factor is formed by the destructive interference between two resonators. Herein, the blue and black lines correspond to the  $Q$  factors of  $\omega_+$  and  $\omega_-$  bands, respectively. Furthermore, as polarization singularities, the topological properties of BICs can be revealed by calculating the far-field polarization states. For more clearness, the far-field polarization states around the BIC in momentum space are shown in Fig. 2(e). It can be seen that the far-field polarization state is undefined at BIC point, which is a polarization singularity in momentum space. Moreover, the position of the BIC can be arbitrarily controlled for different wave vectors by adjusting the interlayer distance. Based on the formation condition of BIC, the dependence of BICs on the interlayer distance  $d$  and  $k_x a/2\pi$  is given by the blue line in Fig. 2(f). Further, we select four points in the blue line and calculate the corresponding  $Q$  factors around the four BIC modes ( $\omega_+$ ), as shown in the inset of Fig. 2(f). When the interlayer distance is  $d = 1.36a$ , the position of BIC can be expected to appear at  $k_x a/2\pi = 0.2$  [corresponding to the red point in Fig. 2(f)]. In general, the BICs will disappear, and the positions of accidental BICs are undefined when the

geometric parameters change. However, by decreasing (increasing) the interlayer distance, the increase (decrease) in propagation phase shift related to the wave vector can be compensated. As a consequence, the position of the BIC can be arbitrarily designed in momentum space.

Based on the formation condition and the conservation of topological charge, we can predict and understand the behaviors of BICs when the parameters of the system are varied. To intuitively show the evolution of BICs that are robust in momentum space, we show the far-field polarization maps of the  $\omega_+$  band at relatively small momentum space in Fig. 3. Our system exhibits  $\{C_{2v}, \sigma_h, T\}$  symmetries, and the typical band structure for  $d/a = 0.68$  is shown in Fig. 3(a). Owing to the non-zero tangential momentum of the wave vector, the dual BICs marked by the red circle will exist at  $k_x a/2\pi = \pm 0.075$  at the symmetric positions in momentum space, as shown in Fig. 3(a). Figure 3(b) gives the polarization vectors together with the  $Q$  factor as the background of the  $\omega_+$  band in momentum space for  $d/a = 0.68$ , where the white arrows represent the distribution of polarization fields. There are two BICs carrying the same topological charges  $q = +1$  on the  $k_x$  axis, and the topological charge can be defined by [29]

$$q = \frac{1}{2\pi} \oint_C d\mathbf{k} \cdot \nabla_{\mathbf{k}} \phi(\mathbf{k}), \quad (5)$$

where  $C$  indicates a closed path in reciprocal space that surrounds the BIC along the counterclockwise direction. Here,  $\phi(\mathbf{k}) = \arg[c_x(\mathbf{k}) + ic_y(\mathbf{k})]$  is the angle of the polarization vector, and  $c_{x,y}(\mathbf{k}) = \iint_{\text{cell}} E_{x,y}^* e^{-ik_x x - ik_y y} dx dy / \iint_{\text{cell}} dx dy$ . In addition, the sign of the component of polarization vectors near the BIC and the polarization vectors winds around the BICs with charge  $q = +1$  are shown in Fig. 3(c). By decreasing  $d/a$ , the dual BICs with the same charges gradually merge to the center in momentum space, as shown in Fig. 3(d). Owing to the conservation of topological charges: annihilation cannot happen



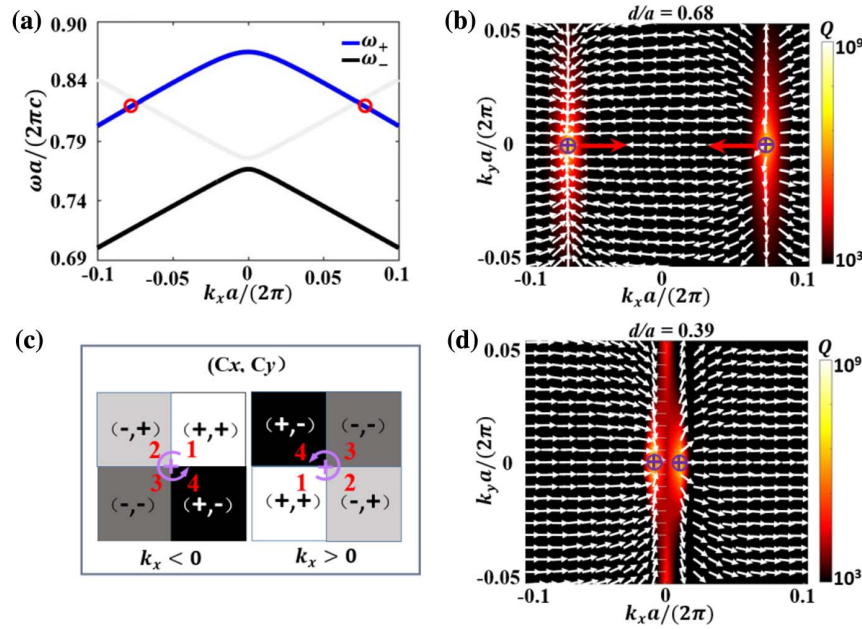


**Fig. 3.** (a) Simulated band structure at  $d/a = 0.68$ . (b) Calculated polarization vectors around BICs with the  $Q$  factors as background in the Brillouin zone for  $d/a = 0.68$ . (c) Sign of polarization vector components around BICs. (d) Calculated polarization vectors around BICs with the  $Q$  factors as background in the Brillouin zone for  $d/a = 0.39$ .

between two BICs with the same charge. It is noted that such accidental BICs are a common wave phenomenon in optical systems, and merging evolution of accidental BICs also exists in other structures [22,29,32,52–54]. Usually, the FW-type accidental BICs come from the coupling between the guided mode resonances and Fabry–Perot modes [32]. Different from the previous works, the formation of a Fabry–Perot type accidental BIC stems from the coupling between two oscillators, and its position is controllable.

### 3. SIMULATION AND EXPERIMENTAL RESULTS

The characteristics of BICs can be observed by measuring the transmission spectra of the structure. To meet the requirement of low refractive index contrast compared to air, the Teflon is used as the dielectric material for grating fabrication in the microwave region. According to the manufacturer datasheet, the relative permittivity of Teflon is  $2 \pm 0.03$  and the loss tangent is  $\tan \delta \approx 1 \times 10^{-3}$  at 30 GHz. It should be pointed out that the material loss would hardly affect the position of BIC, but it would affect the  $Q$  factor of quasi-BIC. The larger the material loss is, the more the decrease of the  $Q$  factor would be. In principle, the size of the structure and operating wavelength can be arbitrarily designed based on the scaling law. In the near-infrared or visible region,  $\text{SiO}_2$  can be used as a candidate material. Owing to the limitation of experimental conditions, as an example, we perform the experiment in the microwave region. We design two samples to observe the properties of BICs. In the two fabricated samples, each grating has the same lattice constant  $a = 7.4$  mm and gap width  $w = 0.5a$ , whereas the interlayer distance  $d$  between the upper and bottom gratings is selected to be 7.35 mm and 9.1 mm, respectively. The sizes of two samples are both 49 cm  $\times$  49 cm, and the size of the

unit cell is smaller than the wavelength. It should be pointed out that the sample size under test is related to the waist of the input beam as it must be shorter than the sample size in order to avoid any undesired diffraction at the edge of the sample. In general, the side length of the sample should be greater than 50 times the incident wavelength. Herein, the side length of the sample is 49 cm, which is 51 times the incident wavelength. In the experiment, the sample is mounted to a holder and fixed on a rotating platform in the middle of two lens antennas. One of the antennas acts as transmitter, and the other works as receiver. Both antennas are connected to a vector network analyzer (VNA, Keysight N5245B) via coaxial cables, and the experimental measurements are performed in an anechoic chamber. The schematic view and photos of the experimental setup and sample are shown in Fig. 4. In fact, the lens antenna can transmit a Gaussian-like beam with a larger waist radius, which has a smaller divergence angle and better angular resolution. Thus, we use a lens antenna rather than a horn antenna as the transmitting and receiving antennas. Of course, the presence of lenses will bring some ripples with noticeable amplitude in the measured  $S$ -parameters because of the multiple reflections between the lenses and the sample under test. To overcome this problem, time-domain gating is applied. The transmission coefficient of the sample can be obtained by measuring the receiving signal ( $S_{21}$ ) with and without the sample.

To determine the position of BIC, we first give the simulated transmittance spectra of the structure along the direction of  $k_x$  at  $d/a = 0.99$ , as shown in Fig. 5(a). One can see that the BIC is located in the vicinity of  $k_x a / 2\pi = 0.122$ , and the simulated transmittance spectra agree well with the band structure in Fig. 2(c). In addition, the far-field polarization of the eigenmode is undefined at BIC point, i.e.,  $S_1 = S_2 = S_3 = 0$  [55], where  $S_{i=1,2,3}$  represent the Stokes parameters. We can

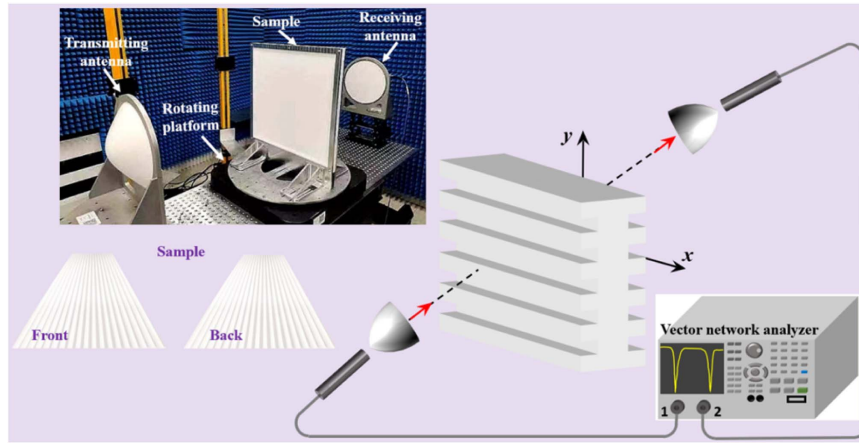


**Fig. 4.** Schematic view and photos of the experimental setup and sample.

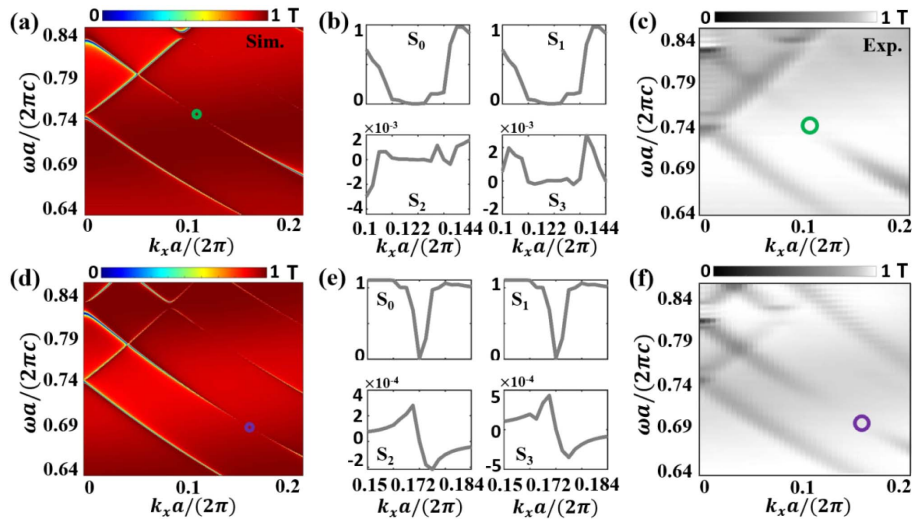


**Fig. 5.** Simulated transmittance spectra of the structure for TM polarization at (a)  $d/a = 0.99$  and (d)  $d/a = 1.23$ . The circles represent the positions of BICs. (b), (e) Corresponding Stokes parameters around BICs points. (c), (f) Corresponding experimental results.

use the polarization-resolved transmission spectra with magnitude and phase at two polarizer angles, i.e., along  $\hat{s}$  and  $\hat{p}$ , to extract the polarization vector fields at the frequency interested. The corresponding Stokes parameters can be written as

$$\begin{aligned} S_0 &= |t_{pp} - t_p|^2 + |t_{sp}|^2, & S_1 &= |t_{pp} - t_p|^2 - |t_{sp}|^2, \\ S_2 &= 2 \operatorname{Re}[(t_{pp} - t_p)t_{sp}^*], & S_3 &= 2 \operatorname{Im}[(t_{pp} - t_p)t_{sp}^*]. \end{aligned} \quad (6)$$

Here,  $t_{sp}$  is the coefficient of transmission converted into the  $s$  polarization for the  $p$ -polarized incident light, and similarly for the other elements.  $t_{pp}$  and  $t_{sp}$  can be extracted from transmission spectra with magnitude and phase, and  $t_p$  for the direct transmission process is obtained by fitting the background in the transmission spectra to the transmission coefficients through a uniform slab with the same thickness and with an effective dielectric constant [56]. The detailed derivation of the above expressions is given in Appendix B. To more

accurately determine the position of the BIC, Fig. 5(b) shows the Stokes parameters at  $d/a = 0.99$ . It is seen that all components of Stokes parameters are equal to zero at  $k_x a / 2\pi = 0.122$ . As a result, the position of BIC can be accurately determined, which is consistent with that in Fig. 2(c). In order to further confirm the theoretical results, we experimentally observe the transmittance spectra of the structure at  $d/a = 0.99$ , as shown in Fig. 5(c). Overall, the measured results agree with the simulated results. Owing to the influence of intrinsic loss and scattering loss induced by fabrication imperfection, the linewidth of the measured transmission spectra is somewhat widened. Furthermore, we set the interlayer distance  $d/a = 1.23$  to observe the properties of BICs. For this structure, the position of the BIC is expected to appear at  $k_x a / 2\pi = 0.172$ , corresponding to the case at the incident angle of  $15^\circ$ . In Fig. 5(d), we show the simulated transmittance spectra of the structure. We see that a BIC occurs in the vicinity of  $k_x a / 2\pi = 0.172$ , and the corresponding measured

transmittance spectra are shown in Fig. 5(f). As predicted, when the interlayer distance  $d/a$  increases, the position of BIC moves along the  $k_x$  axis [in accordance with Fig. 2(f)]. Similarly, all components of Stokes parameters for the second structure are equal to zero for BIC point at  $k_x a/2\pi = 0.172$ , as shown in Fig. 5(e). These findings experimentally demonstrate that the F-P BICs can be accurately designed and observed by demand.

To further demonstrate the topological features of BIC in momentum space, we calculate the far-field polarization states around BIC under different interlayer distances. Here the polarization vectors are calculated from the eigenfields in the unit cell using COMSOL Multiphysics, and the Stokes parameters are  $S_0 = |E_x|^2 + |E_y|^2$ ,  $S_1 = |E_x|^2 - |E_y|^2$ ,  $S_2 = 2 \text{Re}(E_x E_y^*)$ , and  $S_3 = 2 \text{Im}(E_x E_y^*)$ , respectively. Figure 6(a) shows the calculated polarization vectors in momentum space when  $d/a = 0.99$ , where a polarization singularity with charge  $q = +1$  (i.e., BIC) at  $k_x a/2\pi = 0.122$  appears. As  $d/a$  increases from 0.99 to 1.23, the polarization singularity moves along the  $k_x$  axis. In the case of  $d/a = 1.23$ , the polarization singularity is located at  $k_x a/2\pi = 0.172$ , as shown in Fig. 6(c). Utilizing the method of extracting eigenfields, we can theoretically understand the topological characteristics of the BIC in momentum space. Nevertheless, extracting the eigenfields experimentally is quite difficult, particularly in the optical region. As a result, to experimentally observe the topological features of the BIC in momentum space remains a challenge. To reduce the difficulty of the experiment, we propose a general method and rigorous numerical analyses for extracting the polarization vector fields to observe the topological properties of BICs from the polarization-resolved transmission spectra. The detail is given in Appendix B. Based on Eq. (6), Figs. 6(b) and 6(d) give the results of corresponding far-field polarization vectors by extracting the polarization-resolved transmission spectra, which are consistent with the calculated results from the eigenfields. It should be pointed out that the intervals between far-field polarization vectors look larger in comparison to the calculated results from the eigenfields because of a relatively

larger wave vector extraction interval. In a word, the transmission spectra extraction method provides us with a very feasible way to experimentally observe the topological features of BICs.

Now we show that a designed accidental quasi-BIC can be used for highly efficient second harmonic generation (SHG). The schematic of the proposed structure is given in Fig. 7(a). The geometric parameters of the bilayer grating including the lattice constant, height, width, and interlayer distance are  $a = 784$  nm,  $h = 421$  nm,  $w = 228$  nm, and  $d = 776$  nm, respectively. Here the nonlinear material is selected to be LiNbO<sub>3</sub> as it has large second-order nonlinear susceptibilities, and it is highly transparent from the near-infrared to near-ultraviolet region [57–59]. LiNbO<sub>3</sub> is an anisotropy material with a diagonal refractive index distribution of diagonal  $(n_e, n_o, n_o)$  for the optical axis along the  $x$  direction. As shown in Fig. 7(a),  $n_e$  is along the  $x$  direction, and  $n_o$  is along the  $y$  or  $z$  direction. In our calculation, we suppose that  $n_o = n_y = n_z = 2.2264$  and  $n_e = n_x = 2.1506$ , which are obtained in the experiment [60]. According to the formation condition of BIC, one can determine the position of BIC by designing suitable interlayer distance. For instance, when the interlayer distance  $d = 776$  nm and  $m = 1$ , BIC can form at the incident angle  $\theta = 8^\circ$ . Then, we calculate the reflectance spectra of the structure at different incident angles, as shown in Fig. 7(b). It is seen that  $\omega_+$  becomes a BIC with vanishing line width at  $\theta = 8^\circ$ . In the case of  $\theta = 9^\circ$ , the reflectance spectra exhibit dual asymmetric Fano line shapes, which correspond to  $\omega_+$  and  $\omega_-$ . We focus on  $\omega_+$  that corresponds to quasi-BIC, and the corresponding electric field distributions at the  $x$ - $z$  cross section ( $y = a/2$ ) and the  $y$ - $z$  cross section ( $x = a/2$ ) of the unit cell for TM wave are shown in Fig. 7(c). One can see that the electric fields are highly localized inside the structure. The intensity of generated second harmonic light strongly depends on the intensity of the confined electric field within the structure. Owing to its large mode profile volume in bilayer grating when compared with other photonic structures [57–62], a highly efficient SHG would be achieved.

In general, SHG in photonic structure can be characterized as [63]

$$P(2\omega) = \int_V \chi^{(2)}(\mathbf{r}, \omega) [E_{\text{loc}}(\mathbf{r}, \omega)]^2 dV. \quad (7)$$

In Eq. (7),  $\chi^{(2)}(\mathbf{r}, \omega)$  denotes tensor of second-order nonlinear susceptibility,  $E_{\text{loc}}(\mathbf{r}, \omega)$  is the local electric field inside structure, and  $V$  is the volume of a unit cell. Next, we calculate the nonlinear efficiency enhanced by the quasi-BIC based on the second-order polarization density  $(p_x^{\text{SH}}, p_y^{\text{SH}}, p_z^{\text{SH}})$  and the electric field of the pumping light  $(E_x, E_y, E_z)$  in LiNbO<sub>3</sub> as given by

$$\begin{bmatrix} p_x^{\text{SH}} \\ p_y^{\text{SH}} \\ p_z^{\text{SH}} \end{bmatrix} = 2\epsilon_0 \begin{bmatrix} 0 & 0 & 0 & 0 & d_{22} & d_{31} \\ d_{31} & d_{31} & d_{33} & 0 & 0 & 0 \\ d_{22} & 0 & -d_{22} & d_{31} & 0 & 0 \end{bmatrix} \begin{bmatrix} E_x^2 \\ E_y^2 \\ E_z^2 \\ 2E_y E_z \\ 2E_x E_z \\ 2E_x E_y \end{bmatrix}. \quad (8)$$

Herein, the nonlinear coefficients are  $d_{22} = 1.9$  pm/V,  $d_{31} = -3.2$  pm/V, and  $d_{33} = 19.5$  pm/V [60,64],

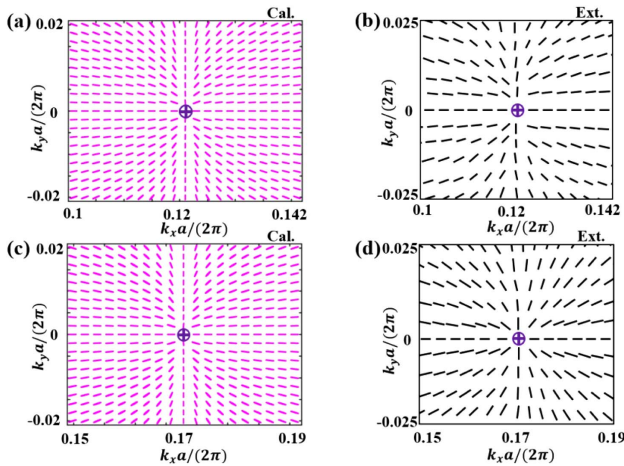


**Fig. 6.** Calculated polarization vectors around BICs in momentum space based on the eigenfield extraction method for (a)  $d/a = 0.99$  and (c)  $d/a = 1.23$ . (b), (d) Corresponding results based on the transmission spectra extraction method.



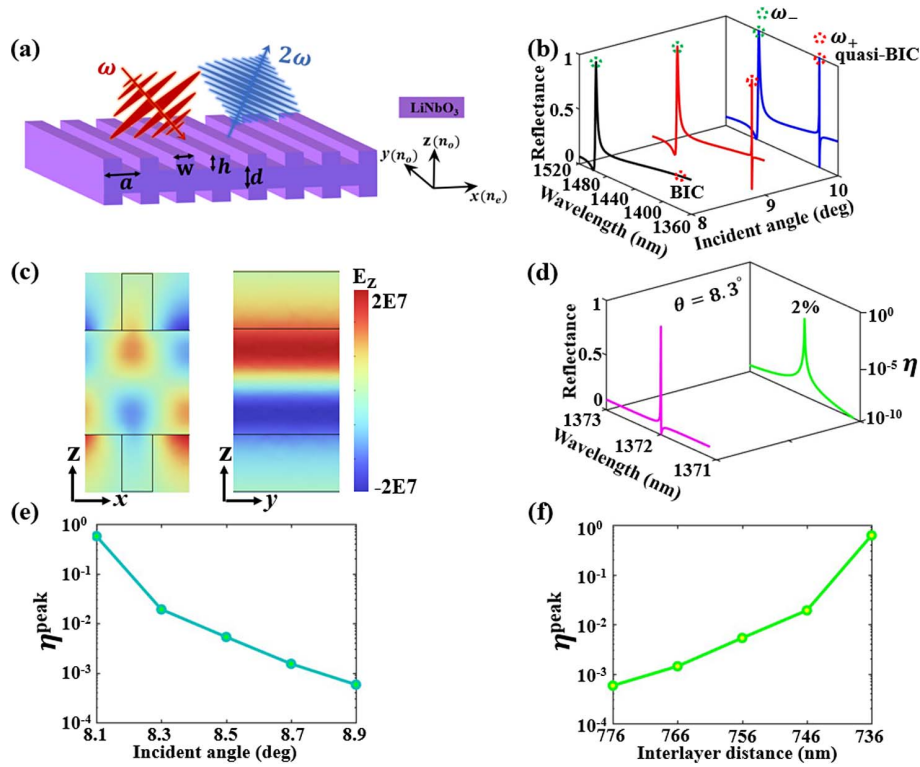


**Fig. 7.** Schematic of the bilayer grating structure for highly efficient SHG. (b) Reflectance spectra of the structure at different incident angles for TM polarization. (c) Electric field distributions at the  $x$ - $z$  cross section ( $y = a/2$ ) and the  $y$ - $z$  cross section ( $x = a/2$ ) at the wavelength of quasi-BIC at  $\theta = 9^\circ$ . (d) Calculated reflectance and SHG conversion efficiency versus the wavelength of pumping light at  $\theta = 8.3^\circ$ . (e) Dependence of the SHG conversion efficiency on the incident angle. (f) Dependence of the SHG conversion efficiency on the interlayer distance at  $\theta = 8.9^\circ$ .

respectively. The SHG conversion efficiency can be written as  $\eta = P_{\text{SHG}}/P_{\text{in}}$ . Figure 7(d) shows the calculated reflectance and SHG conversion efficiency versus the wavelength of pumping light at  $\theta = 8.3^\circ$ . Assisted by quasi-BIC, the SHG conversion efficiency reaches 2% under pumping intensity  $I_0 = 1 \text{ MW/cm}^2$ . In addition, we calculate the dependence of the SHG conversion efficiency on the incident angle, as shown in Fig. 7(e). When  $\theta = 8.9^\circ$ , the SHG conversion efficiency is only 0.02%. As  $\theta$  gradually approaches  $8^\circ$  (BIC condition), the SHG conversion efficiency increases significantly. When  $\theta = 8.1^\circ$ , the SHG conversion efficiency reaches 57.4%. Similarly, we calculate the dependence of the SHG conversion efficiency on the interlayer distance at  $\theta = 8.9^\circ$ , as shown in Fig. 7(f). As the interlayer distance decreases from 776 to 736 nm (approaching the BIC condition at  $\theta = 8.9^\circ$ ), the SHG conversion efficiency rapidly increases from 0.02% to 61.5%. Overall, a highly efficient SHG can be achieved in a wide parameter space, owing to the high  $Q$  factor and large mode profile volume of the designed quasi-BIC.

#### 4. CONCLUSION

In conclusion, an accurately designed accidental BIC in a coupled-resonators system consisting of the bilayer grating is theoretically and experimentally investigated. We show that the position of the BIC can be arbitrarily controlled in

momentum space by changing the interlayer distance between the gratings to tune the propagation phase shift related with the wave vector. Besides, we propose a general method for extracting the polarization vector fields to observe the topological properties of BICs. As an example of an application, the highly efficient SHG assisted by the quasi-BIC is also given. Besides highly efficient SHG, these freely designed BICs in momentum space would be very useful for the design of high-efficiency filters, ultrasensitive sensors, and so on.

#### APPENDIX A: FITTING REFLECTANCE SPECTRA BY THE SINGLE RESONATOR MODEL

The optical response of single grating can be described by the single resonator model (SRM) around the angular frequency of the guided mode resonance (GMR). Figure 8 shows the calculated and fitted reflectance spectra by SRM.

#### APPENDIX B: EXTRACTION OF POLARIZATION VECTOR FIELDS FROM TRANSMISSION SPECTRA

We can use the polarization-resolved transmission spectra to extract the polarization vector fields of the band of interest.

Here we consider a system with two-fold in-plane rotational symmetry and mirror symmetry  $\sigma_z$ , as illustrated in Fig. 9. Under these conditions the column vectors  $\mathbf{s}^+$  and  $\mathbf{s}^-$

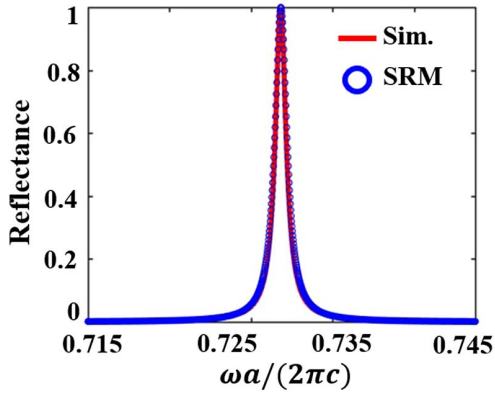


**Fig. 8.** Reflectance spectrum of the single grating for TM polarization at  $k_x a / 2\pi = 0.122$ . Red solid line represents the calculated reflectance spectra. Blue circle denotes the fitting reflectance spectrum based on SRM.

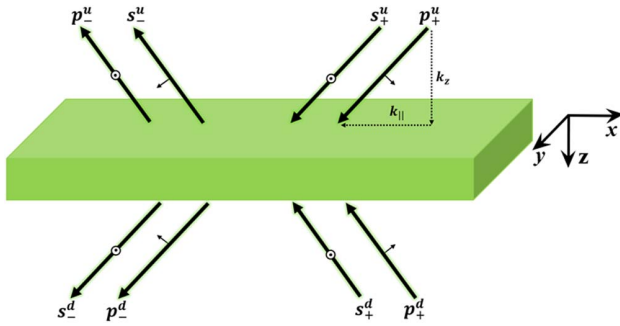


**Fig. 9.** Schematic of a system with two-fold in-plane rotational symmetry and mirror-symmetry along  $z$ .

describing the incoming and outgoing electric field vectors can

be written as  $\mathbf{s}^+ = \begin{pmatrix} E_s^{u+} \\ E_s^{d+} \\ E_p^{u+} \\ E_p^{d+} \end{pmatrix}$ ,  $\mathbf{s}^- = \begin{pmatrix} E_s^{u-} \\ E_s^{d-} \\ E_p^{u-} \\ E_p^{d-} \end{pmatrix}$ , where sub-

scripts  $s$  and  $p$  denote the TE and TM polarizations, respectively, and the superscripts  $u$  and  $d$  denote the waves in the upper and lower half-spaces with respect to the structure. Considering TM polarization incidence from upper half-space, the incoming electric field vector can be expressed as

$$\mathbf{s}^+ = \begin{pmatrix} 0 \\ 0 \\ E_p^{u+} \\ 0 \end{pmatrix} = \sqrt{I_0} e^{i\phi_0} \begin{pmatrix} 0 \\ 0 \\ 1 \\ 0 \end{pmatrix}. \quad (\text{B1})$$

The corresponding outgoing electric field vector can be written as

$$\mathbf{s}^- = \sqrt{I_0} e^{i\phi_0} \mathbf{S} \begin{pmatrix} 0 \\ 0 \\ 1 \\ 0 \end{pmatrix}, \quad (\text{B2})$$

where  $\mathbf{S}$  is the scattering matrix of the system. Generally,  $\mathbf{S}$  can be decomposed into two parts:  $\mathbf{S} = \mathbf{C} + \mathbf{C}_r$ , where  $\mathbf{C}$  and  $\mathbf{C}_r$

describe the non-resonant process and resonant process for scattering, respectively. For a non-resonant system,  $\mathbf{S}$  can be written as

$$\mathbf{S} = \mathbf{C} = \begin{pmatrix} r_s & t_s & 0 & 0 \\ t_s & r_s & 0 & 0 \\ 0 & 0 & r_p & t_p \\ 0 & 0 & t_p & r_p \end{pmatrix}, \quad (\text{B3})$$

while a resonant system has a scattering matrix that can be expressed as

$$\mathbf{S} = \begin{pmatrix} r_{ss} & t_{ss} & r_{sp} & t_{sp} \\ t_{ss} & r_{ss} & t_{sp} & r_{sp} \\ r_{ps} & t_{ps} & r_{pp} & t_{pp} \\ t_{ps} & r_{ps} & t_{pp} & r_{pp} \end{pmatrix}. \quad (\text{B4})$$

One can clearly see that the off-diagonal  $2 \times 2$  blocks represent individual contributions from resonance. Substituting Eq. (B4) into Eq. (B2) produces

$$\mathbf{s}^- = \sqrt{I_0} e^{i\phi_0} \mathbf{S} \begin{pmatrix} r_{sp} \\ t_{sp} \\ r_{pp} \\ t_{pp} \end{pmatrix}. \quad (\text{B5})$$

We only consider the transmission spectra, so  $\mathbf{s}^-$  can be simplified as

$$\mathbf{E}^{d-} = \sqrt{I_0} e^{i\phi_0} \begin{pmatrix} t_{sp} \\ t_{pp} \end{pmatrix}. \quad (\text{B6})$$

Here  $\mathbf{E}^{d-}$  represents the outgoing electric field vectors in the lower half-space of the structure. Considering the effect of analyzers:

$$\mathbf{E}^{d-} \cdot \hat{\tau} = [(\hat{\tau} \cdot \hat{s})t_{sp} + (\hat{\tau} \cdot \hat{p})t_{pp}] \sqrt{I_0} e^{i\phi_0}, \quad (\text{B7})$$

where  $\hat{\tau}$  is the unit vector of the polarization analysis along the  $\hat{p}$ , the intensity received by the receiver is

$$I = I_0 |(\hat{\tau} \cdot \hat{s})t_{sp} + (\hat{\tau} \cdot \hat{p})t_{pp}|^2. \quad (\text{B8})$$

Normalized by  $I_0$ , the transmittance of system for TM polarization incidence can be written as

$$T_p = |(\hat{\tau} \cdot \hat{s})t_{sp} + (\hat{\tau} \cdot \hat{p})t_{pp}|^2. \quad (\text{B9})$$

If we adjust  $\hat{\tau}$  along the  $\hat{s}$ ,  $\hat{p}$ , the corresponding transmittance is  $T_{sp} = |t_{sp}|^2$ ,  $T_{pp} = |t_{pp}|^2$ , respectively. In general, Jones vectors can be defined by two orthogonal polarization vectors. For convenience, we choose  $\hat{s}$  and  $\hat{p}$  as basis, and the corresponding Stokes parameters can be written as

$$\begin{aligned} \tilde{S}_0 &= T_{pp} + T_{sp} = |t_{pp}|^2 + |t_{sp}|^2, \\ \tilde{S}_1 &= T_{pp} - T_{sp} = |t_{pp}|^2 - |t_{sp}|^2, \\ \tilde{S}_2 &= 2 \operatorname{Re}(t_{pp} t_{sp}^*), \\ \tilde{S}_3 &= 2 \operatorname{Im}(t_{pp} t_{sp}^*), \end{aligned} \quad (\text{B10})$$

where “\*” denotes complex conjugate. It is noted that the expression above represents the polarization vectors contributed by direct process and resonance. As a result,  $\tilde{S}_{i=0,1,2,3}$  represent the polarization vectors of non-eigenstates. Based on Eqs. (B3) and (B4), the contribution from the direct process to getting



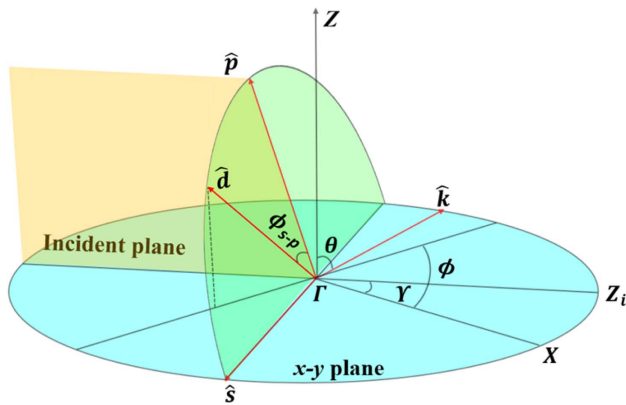


**Fig. 10.** Schematic illustration for the relevant angles and vectors in determining the polarization vector and its projection onto the  $x$ - $y$  plane.

polarization vectors of eigenstates should be subtracted. Thus, the Stokes parameters can be defined as

$$\begin{aligned} S_0 &= |t_{pp} - t_p|^2 + |t_{sp}|^2, & S_1 &= |t_{pp} - t_p|^2 - |t_{sp}|^2, \\ S_2 &= 2 \operatorname{Re}[(t_{pp} - t_p)t_{sp}^*], & S_3 &= 2 \operatorname{Im}[(t_{pp} - t_p)t_{sp}^*]. \end{aligned} \quad (\text{B11})$$

Here  $t_{sp}$  is the coefficient of transmission converted into the  $s$  polarization for the  $p$ -polarized incident light, and similarly for the other elements.  $t_{pp}$  and  $t_{sp}$  can be extracted from transmission spectra with magnitude and phase, and  $t_p$  for the direct transmission process is formed by fitting the background in the transmission spectra to the transmission coefficients through a uniform slab with the same thickness and with an effective dielectric constant.

To determine the far-field polarization states, we need to get the polarization-resolved transmission spectra with magnitude and phase at two polarizer angles, i.e., along  $\hat{s}$  and  $\hat{p}$ . The schematic view of determining the projection of polarization vector is shown in Fig. 10. Here we define the polarization state of the resonant radiation as  $\hat{d}$ . The two axes of polarizations are  $\hat{s}$  and  $\hat{p}$ , determined by the incident plane and propagation direction  $\hat{k}$ . The angle between the  $z$  axis and  $\hat{k}$  is denoted by  $\theta$ . Additionally, we determine  $\phi_{s-p}$  as the angle of polarization vector  $\hat{d}$  relative to  $\hat{p}$  in  $\hat{s}$ - $\hat{p}$  plane and  $Y$  as the angle between the  $\Gamma Z_i$  and the  $\Gamma X$  directions in momentum space. Generally speaking, polarization states of radiation are elliptical except high-symmetry directions. Owing to the  $180^\circ$  rotational symmetry  $C_2$  of the structure, these polarization states are close to linear polarization [65]. We regard approximately polarization states as linear polarization. The angle  $\phi_{s-p}$  can be expressed as

$$\phi_{s-p} = \frac{1}{2 \arg(S_1 + iS_2)}. \quad (\text{B12})$$

Since the  $\hat{s}$ - $\hat{p}$  plane rotates with incident plane, we project the polarization vector onto the  $x$ - $y$  plane. The corresponding geometric relation is

$$\varphi = Y + \arctan\left(\frac{\tan \phi_{s-p}}{\cos \theta}\right). \quad (\text{B13})$$

Here  $\varphi$  denotes the angle of projected polarization vector relative to  $\Gamma X$  direction.

**Funding.** National Key Research and Development Program of China (2021YFA1400602, 2021YFA1400603, 2022YFA1404800); National Natural Science Foundation of China (12274325, 12234007, 12221004, 12004284, 11974261, 91850206); Major Program of National Natural Science Foundation of China (91963212); Science and Technology Commission of Shanghai Municipality (22142200400, 21DZ1101500, 2019SHZDZX01); Basic and Applied Basic Research Foundation of Guangdong Province (2023A1515011024).

**Disclosures.** The authors state no conflicts of interest.

**Data Availability.** Data underlying the results presented in this paper are not publicly available at this time but may be obtained from the authors upon reasonable request.

## REFERENCES

- C. W. Hsu, B. Zhen, A. D. Stone, *et al.*, "Bound state in the continuum," *Nat. Rev. Mater.* **1**, 16048 (2019).
- J. von Neumann and E. P. Wigner, "Über merkwürdige diskrete eigenwerte," *Phys. Z.* **30**, 465 (1929).
- H. Friedrich and D. Wintgen, "Interfering resonances and bound states in the continuum," *Phys. Rev. A* **32**, 3231-3242 (1985).
- C. M. Linton and P. McIver, "Embedded trapped modes in water waves and acoustics," *Wave Motion* **45**, 16-29 (2007).
- H. Krüger, "On the existence of embedded eigenvalues," *J. Math. Anal. Appl.* **395**, 776-787 (2012).
- D. C. Marinica, A. G. Borisov, and S. V. Shabanov, "Bound states in the continuum in photonics," *Phys. Rev. Lett.* **100**, 183902 (2008).
- W. Liu, B. Wang, Y. Zhang, *et al.*, "Circularly polarized states spawning from bound states in the continuum," *Phys. Rev. Lett.* **123**, 116104 (2019).
- S. G. Tikhodeev, A. L. Yablonskii, E. A. Muljarov, *et al.*, "Quasiguidded modes and optical properties of photonic crystal slabs," *Phys. Rev. B* **66**, 045102 (2002).
- A. Christ, S. G. Tikhodeev, N. A. Gippius, *et al.*, "Waveguide-plasmon polaritons: strong coupling of photonic and electronic resonances in a metallic photonic crystal slab," *Phys. Rev. Lett.* **91**, 183901 (2003).
- K. Koshelev, S. Lepeshov, M. Liu, *et al.*, "Asymmetric metasurfaces with high-Q resonances governed by bound states in the continuum," *Phys. Rev. Lett.* **121**, 193903 (2018).
- L. Cong and R. Singh, "Symmetry-protected dual bound states in the continuum in metamaterials," *Adv. Opt. Mater.* **7**, 1900383 (2019).
- A. Kodigala, T. Lepetit, Q. Gu, *et al.*, "Lasing action from photonic bound states in continuum," *Nature* **541**, 196-199 (2017).
- Q. Song, J. Hu, S. Dai, *et al.*, "Coexistence of a new type of bound state in the continuum and a lasing threshold mode induced by PT symmetry," *Sci. Adv.* **6**, eabc1160 (2020).
- H. Zhong, Y. Yu, Z. Zheng, *et al.*, "Ultra-low threshold continuous-wave quantum dot mini-BIC lasers," *Light Sci. Appl.* **12**, 100 (2023).
- S. Romano, G. Zito, S. Torino, *et al.*, "Label-free sensing of ultralow-weight molecules with all dielectric metasurfaces supporting bound states in the continuum," *Photonics Res.* **6**, 726-733 (2018).
- T. C. Tan, Y. K. Srivastava, R. T. Ako, *et al.*, "Active control of nano-dielectric-induced THz quasi-BIC in flexible metasurfaces: a platform for modulation and sensing," *Adv. Mater.* **33**, 2100836 (2021).
- F. Wu, J. Wu, Z. Guo, *et al.*, "Giant Enhancement of the Goos-Hänchen shift assisted by quasibound states in the continuum," *Phys. Rev. Appl.* **12**, 014028 (2019).
- X. Yin, J. Jin, M. Soljačić, *et al.*, "Observation of topologically enabled unidirectional guided resonances," *Nature* **580**, 467-471 (2020).

19. C. Zhao, G. Hu, Y. Chen, *et al.*, "Unidirectional bound states in the continuum in Weyl semimetal nanostructures," *Photonics Res.* **10**, 1828–1838 (2022).
20. G. Zograf, K. Koshelev, A. Zalogina, *et al.*, "High-harmonic generation from resonant dielectric metasurfaces empowered by bound states in the continuum," *ACS Photonics* **9**, 567–574 (2022).
21. T. Liu, M. Qin, F. Wu, *et al.*, "High-efficiency optical frequency mixing in all-dielectric metasurface enabled by multiple bound states in the continuum," *Phys. Rev. B* **107**, 075441 (2023).
22. X. Qi, J. Wu, F. Wu, *et al.*, "Steerable merging bound states in the continuum on a quasi-flatband of photonic crystal slab without breaking symmetry," *Photonics Res.* **11**, 1262–1274 (2023).
23. M. V. Gorkunov, A. A. Antonov, and Y. S. Kivshar, "Metasurfaces with maximum chirality empowered by bound states in the continuum," *Phys. Rev. Lett.* **125**, 093903 (2020).
24. A. Overvig, N. Yu, and A. Alù, "Chiral quasi-bound states in the continuum," *Phys. Rev. Lett.* **126**, 073001 (2021).
25. J. Wu, X. Xu, X. Su, *et al.*, "Observation of giant extrinsic chirality empowered by quasi-bound states in the continuum," *Phys. Rev. Appl.* **16**, 064018 (2021).
26. X. Zhang, Y. Liu, J. Han, *et al.*, "Chiral emission from resonant metasurface," *Science* **377**, 1215–1218 (2022).
27. Y. Lim, I. C. Seo, S.-C. An, *et al.*, "Maximally chiral emission via chiral quasibound states in the continuum," *Laser Photonics Rev.* **17**, 2200611 (2023).
28. Y. Chen, H. Deng, X. Sha, *et al.*, "Observation of intrinsic chiral bound states in the continuum," *Nature* **613**, 474–478 (2023).
29. B. Zhen, C. W. Hsu, L. Lu, *et al.*, "Topological nature of optical bound states in the continuum," *Phys. Rev. Lett.* **113**, 257401 (2014).
30. M. Kang, S. Zhang, M. Xiao, *et al.*, "Merging bound states in the continuum at off-high symmetry points," *Phys. Rev. Lett.* **126**, 117402 (2021).
31. Y. Zeng, G. Hu, K. Liu, *et al.*, "Dynamics of topological polarization singularity in momentum space," *Phys. Rev. Lett.* **127**, 176101 (2021).
32. P. Hu, J. Wang, Q. Jiang, *et al.*, "Global phase diagram of bound states in the continuum," *Optica* **9**, 1353–1361 (2022).
33. X. Wang, J. Wang, X. Zhao, *et al.*, "Realizing tunable evolution of Bound states in the continuum and circular polarized points by symmetry breaking," *ACS Photonics* **10**, 2316–2322 (2023).
34. K. Koshelev, A. Bogdanov, and Y. Kivshar, "Meta-optics and bound states in the continuum," *Sci. Bull.* **64**, 836–842 (2019).
35. C. F. Doiron, I. Brener, and A. Cerjan, "Realizing symmetry-guaranteed pairs of bound states in the continuum in metasurfaces," *Nat. Commun.* **13**, 7534 (2022).
36. S. Yang and J. C. Ndukaife, "Optofluidic transport and assembly of nanoparticles using an all-dielectric quasi-BIC metasurface," *Light Sci. Appl.* **12**, 2047 (2023).
37. C. Zhou, L. Huang, R. Jin, *et al.*, "Bound states in the continuum in asymmetric dielectric metasurfaces," *Laser Photonics Rev.* **17**, 2200564 (2023).
38. J. Wang, L. Shi, and J. Zi, "Spin Hall effect of light via momentum-space topological vortices around bound states in the continuum," *Phys. Rev. Lett.* **129**, 236101 (2022).
39. H. Qin, Y. Shi, Z. Su, *et al.*, "Exploiting extraordinary topological forces at bound states in the continuum," *Sci. Adv.* **8**, eade75556 (2022).
40. W. Wang, Y. K. Srivastava, T. C. Tan, *et al.*, "Brillouin zone folding driven bound states in the continuum," *Nat. Commun.* **14**, 2811 (2023).
41. P. Hu, C. Xie, Q. Song, *et al.*, "Bound states in the continuum based on the total internal reflection of Bloch waves," *Natl. Sci. Rev.* **10**, nwac043 (2023).
42. Z. F. Sadrieva, I. S. Sinev, K. L. Koshelev, *et al.*, "Transition from optical bound states in the continuum to leaky resonances: role of substrate and roughness," *ACS Photonics* **4**, 723–727 (2017).
43. E. N. Bulgakov, D. N. Maksimov, P. N. Semina, *et al.*, "Propagating bound states in the continuum in dielectric gratings," *J. Opt. Soc. Am. B* **35**, 1218–1222 (2018).
44. W. Shi, J. Gu, X. Zhang, *et al.*, "Terahertz bound states in the continuum with incident angle robustness induced by a dual period meta-grating," *Photonics Res.* **10**, 810–819 (2022).
45. E. N. Bulgakov and A. F. Sadreev, "Bound states in the continuum in photonic waveguides inspired by defects," *Phys. Rev. B* **78**, 075105 (2008).
46. Q. Zhou, Y. Fu, L. Huang, *et al.*, "Geometry symmetry-free and higher-order optical bound states in the continuum," *Nat. Commun.* **12**, 4390 (2021).
47. F. Wu, C. Fan, K. Zhu, *et al.*, "Tailoring electromagnetic responses in a coupled-grating system with combined modulation of near-field and far-field couplings," *Phys. Rev. B* **105**, 245417 (2022).
48. S. I. Azzam, V. M. Shalaev, A. Boltasseva, *et al.*, "Formation of bound states in the continuum in hybrid plasmonic-photonic systems," *Phys. Rev. Lett.* **121**, 253901 (2018).
49. T. Dong, J. Liang, S. Camayd-Munoz, *et al.*, "Ultra-low-loss on-chip zero-index materials," *Light Sci. Appl.* **10**, 10 (2021).
50. J. Wu, Q. Wei, F. Wu, *et al.*, "On-chip multiple beam splitting assisted by bound states in the continuum," *Opt. Lett.* **47**, 3135–3138 (2022).
51. L. Gu, H. Fang, J. Li, *et al.*, "A compact structure for realizing Lorentzian, Fano, Fano and electromagnetically induced transparency resonance lineshapes in a microring resonator," *Nanophotonics* **8**, 841–848 (2019).
52. K. Wang, H. Liu, Z. Li, *et al.*, "All-dielectric metasurface-based multi-mode sensing with symmetry-protected and accidental bound states in the continuum," *Results Phys.* **46**, 106276 (2023).
53. H. Zhang, K. Wang, Z. Li, *et al.*, "Perfect narrowband circular dichroism based on intrinsic chiral dual quasi-bound states in the continuum in terahertz metasurfaces," *Results Phys.* **52**, 106885 (2023).
54. H. Liu, K. Wang, H. Ma, *et al.*, "Switchable optical vortex beam generator based on an all-dielectric metasurface governed by merging bound states in the continuum," *Opt. Express* **31**, 19159–19172 (2023).
55. Y. Zhang, A. Chen, W. Liu, *et al.*, "Observation of polarization vortices in momentum space," *Phys. Rev. Lett.* **120**, 186103 (2018).
56. S. Fan, W. Suh, and J. D. Joannopoulos, "Temporal coupled mode theory for the Fano resonance in optical resonators," *J. Opt. Soc. Am. A* **20**, 569–572 (2003).
57. Z. Yu and X. Sun, "Acousto-optic modulation of photonic bound state in the continuum," *Light Sci. Appl.* **9**, 1 (2020).
58. Z. Huang, K. Luo, Z. Feng, *et al.*, "Resonant enhancement of second harmonic generation in etchless thin film lithium niobate heteronanostructure," *Sci. China Phys. Mech. Astron.* **65**, 104211 (2022).
59. S. Wu, W. Song, J. Sun, *et al.*, "Broadband asymmetric light transport in compact lithiumniobate waveguides," *Laser Photonics Rev.* **17**, 2300306 (2023).
60. D. E. Zelmon, D. L. Small, and D. Jundt, "Infrared corrected Sellmeier coefficients for congruently grown lithium niobite and 5 mol. % magnesium oxide-doped lithium niobite," *J. Opt. Soc. Am. B* **14**, 3319–3322 (1997).
61. S. Cai, S. Zong, X. Liu, *et al.*, "Efficiently spatial field localization enabled second-harmonic and sum-frequency generation in an etchless LiNbO<sub>3</sub> layer by guided resonant quasi-bound states in the continuum," *Appl. Phys. Lett.* **123**, 111701 (2023).
62. S. Feng, T. Liu, W. Chen, *et al.*, "Enhanced sum-frequency generation from etchless lithium niobite empowered by dual quasi-bound states in the continuum," *Sci. China Phys. Mech. Astron.* **66**, 124214 (2023).
63. Y. Yang, W. Wang, A. Boulesbaa, *et al.*, "Nonlinear Fano-resonant dielectric metasurfaces," *Nano Lett.* **15**, 7388–7393 (2015).
64. Z. Zheng, L. Xu, L. Huang, *et al.*, "Boosting second-harmonic generation in the LiNbO<sub>3</sub> metasurface using high-Q guided resonances and bound states in the continuum," *Phys. Rev. B* **106**, 125411 (2022).
65. C. W. Hsu, B. Zhen, M. Soljačić, *et al.*, "Polarization state of radiation from a photonic crystal slab," *arXiv*, arXiv:1708.02197 (2017).